

Performance of Steel Moment Connections under a Column Removal Scenario. II: Analysis

Fahim Sadek, Ph.D., M.ASCE¹, Joseph A. Main, Ph.D., A.M.ASCE²,
H. S. Lew, Ph.D., P.E., F.ASCE³, and Sherif El-Tawil, Ph.D., P.E., F.ASCE⁴

Abstract: This paper presents a computational investigation of the response of steel beam-column assemblies with moment connections under monotonic loading conditions simulating a column removal scenario. Two beam-column assemblies are analyzed, which incorporate (1) welded unreinforced flange, bolted web connections and (2) reduced beam section connections. Detailed models of the assemblies are developed, which use highly refined solid and shell elements to represent nonlinear material behavior and fracture. Reduced models are also developed, which use a much smaller number of beam and spring elements and are intended for use in future studies to assess the vulnerability of complete structural systems to disproportionate collapse. The two modeling approaches are described, and computational results are compared with the results of full-scale tests described in the companion paper. Good agreement is observed, demonstrating that both the detailed and reduced models are capable of capturing the predominant response characteristics and failure modes of the assemblies, including the development of tensile forces associated with catenary action and the ultimate failure of the moment connections under combined bending and axial stresses.

CE Database subject headings: Buildings; Connections; Finite element method; Nonlinear analysis; Progressive collapse; Seismic design; Steel structures.

¹ Leader, Structures Group, Engineering Laboratory, National Institute of Standards and Technology, Gaithersburg, MD 20899-8611, fahim.sadek@nist.gov

² Research Structural Engineer, Engineering Laboratory, National Institute of Standards and Technology, Gaithersburg, MD 20899-8611, joseph.main@nist.gov

³ Senior Research Structural Engineer, Engineering Laboratory, National Institute of Standards and Technology, Gaithersburg, MD 20899-8611, hsl@nist.gov

⁴ Professor, Department of Civil and Environmental Engineering, University of Michigan, Ann Arbor, MI 48109-2125, eltawil@umich.edu.

Introduction

Disproportionate collapse is widespread failure of a structure that results from localized initial damage (e.g., failure of a column), in which the final extent of damage far exceeds the initial extent. An accurate characterization of the nonlinear, large-deformation behavior associated with the redistribution of loads in such local damage scenarios is critical in assessing the potential for disproportionate collapse. The National Institute of Standards and Technology (NIST) is conducting research to develop reliable methodologies for assessing the vulnerability of structures to disproportionate collapse and for quantifying the reserve capacity and robustness of structures at the system level. This research involves the development of three-dimensional models of various types of structural systems, which must be capable of representing the predominant response characteristics and failure modes of each structural system. This paper focuses on the analysis of steel moment frames under a column removal scenario.

Two basic modeling approaches can be considered for collapse analysis of structural systems: (1) detailed finite element modeling, which uses highly refined solid and/or shell element meshes to represent nonlinear material behavior and fracture, and (2) reduced finite element modeling, which uses a much smaller number of beam and spring elements. Reduced models can be analyzed much more rapidly than detailed models, making them well suited for collapse analysis of complete structural systems.

A number of previous studies have used detailed and/or reduced modeling approaches for collapse analysis of steel framing systems. Khandelwal and El-Tawil (2007) used detailed models to study the behavior of special moment frames (SMFs) with reduced beam section (RBS) connections. Khandelwal et al. (2008) used reduced models to analyze SMFs with RBS connections as well as intermediate moment frames (IMFs) with welded unreinforced flange,

welded web (WUF-W) connections. Sadek et al. (2008) and Alashker et al. (2010) used both detailed and reduced models to study single-plate shear connections, while Khandelwal et al. (2009) and Khandelwal and El-Tawil (2011) used reduced models to analyze steel braced frames. While these studies considered column removal scenarios, other studies have focused on the development of reduced models to represent the moment-rotation behavior of connections. Del Savio et al. (2009) present a reduced modeling approach to represent the interaction of axial force and bending moment for end plate and web cleat connections. Yim and Krauthammer (2010) used a reduced modeling approach to represent the moment-rotation behavior of welded unreinforced flange, bolted web (WUF-B) connections and compared the reduced model predictions with results from detailed models. Alashker et al. (2011) investigated how various levels of approximations in collapse modeling influence the modeled response.

Because of the complexities of the nonlinear behavior that connections exhibit under collapse scenarios, physical tests are indispensable for establishing confidence in both detailed and reduced modeling approaches. A companion paper (Lew et al. 2012), describes full-scale testing of two steel beam-column assemblies, each comprising three columns and two beams. One specimen represents part of a seismically designed intermediate moment frame (IMF), incorporating welded unreinforced flange, bolted web (WUF-B) connections, and the other represents part of a special moment frame (SMF), incorporating reduced beam section (RBS) connections. In this paper, both detailed and reduced models are developed of these two test specimens, and the computational results are compared with the experimental measurements. The finite element analyses presented in this study are conducted using explicit time integration in LS-DYNA (Hallquist 2007), a general-purpose finite element software package. The analyses account for both geometrical and material nonlinearities, including fracture. In all analyses the

center stub column is pushed downward under displacement control using a pre-defined displacement time-history curve until failure occurs. Displacements are increased at a slow rate to minimize dynamic effects, similar to the test conditions.

Description of Test Specimens

The full-scale test specimens described in Lew et al. (2012) consisted of two beam spans connected to three columns using moment connections. The span length of the beams (center-to-center of columns) was 6.10 m. The beams selected for the first specimen were W21x73 sections and were connected to W18x119 columns using WUF-B connections. The WUF-B connection included a shear plate (shear tab) that was fillet welded to the column flange and bolted to the beam web using three 25 mm diameter, high strength bolts. The beam flanges were joined to the column flange using complete joint penetration (CJP) groove welds. Continuity plates were provided for both interior and exterior columns. The beams selected for the second specimen were W24x94 sections and were connected to W24x131 columns using RBS connections. The beam flanges and web were connected to the column flange using CJP groove welds. The RBS connections utilized circular radius cuts in both top and bottom flanges of the beam at a distance from the beam-column interface. Continuity plates were provided for both center and end columns, while doubler plates were required only for the center column. ASTM A992 structural steel ($F_y = 345$ MPa) was used in all beams, columns, and doubler plates in the panel zone. ASTM A36 steel ($F_y = 248$ MPa) was used for the shear tabs and continuity plates at connections and ASTM A490 high strength bolts were used for the bolted connections.

For both specimens, the tops of the two end columns were restrained by two diagonal braces for each column. The diagonal braces simulated the bracing effect provided by the upper floors in a multi-story building. A pair of columns straddling each beam at mid-span provided

lateral bracing for the beams. The vertical load was applied to the top of the center stub column by a single hydraulic ram acting through a load cell and a steel plate. A pair of steel plates on each side of the center stub column restrained out-of-plane motion at the lower end of the center stub column.

Modeling Approach

For each test specimen, both detailed and reduced models were developed. This section describes the general approach used to represent the various materials and components of the test specimens in the detailed and reduced models. Subsequent sections provide further information on the models of each test specimen.

Steel Material Models

Various material models are available in LS-DYNA that can capture the nonlinear behavior and failure of the steel components. The primary material model used in the analyses presented in this study was a piecewise linear plasticity model (material model 24 in LS-DYNA; Hallquist 2007). In this model, an effective stress versus effective plastic strain curve is specified, along with a plastic strain to failure. Fracture is simulated using element erosion, in which elements are removed from the model (i.e., their stiffness drops to zero) when the specified failure strain is reached.

For the various types of steel used in the test specimens, the material model parameters were developed based on engineering stress-strain curves obtained from coupon tensile tests for all steel sections and plates. The coupon tensile tests applied the ASTM 370 test standard (ASTM 2003). For both the WUF-B and RBS specimens, the coupon tests provided data for

beam webs, beam flanges, column webs, column flanges, shear tabs, continuity plates, and any doubler plates.

For the solid and shell elements used in the detailed models, engineering stress-strain curves from coupon tensile tests were converted to true stress vs. plastic strain curves, and the resulting true stress-strain curves were extrapolated linearly beyond the point of necking onset. The post-necking tangent modulus and the failure strain ε_f were adjusted to achieve quantitative agreement between measured and calculated engineering stress-strain curves in the softening region beyond the ultimate stress. Due to mesh-size sensitivity in the modeling of softening behavior, finite element models of tensile coupons were developed using the same mesh size and type (shell or solid element) as those used in the various models of the test specimens for each steel type. This approach ensured that the measured nonlinear material behavior up to failure was accurately captured in the material model.

Because stress calculations for the beam elements used in the reduced models do not incorporate changes in cross-sectional area due to axial strain, stress-strain curves for the beam material models were defined using engineering stress values, rather than true stress values. The corresponding plastic strain values were adjusted so that the engineering stress-strain curves obtained computationally from uniaxial tension matched those obtained experimentally. Values of ε_f for a particular beam element size were determined such that the extension at fracture was consistent with the results of a detailed solid or shell element model with a corresponding gage length.

Fig. 1 shows examples of detailed finite element models of a tensile coupon obtained from the flanges of the W21x73 beam section used in the WUF-B specimen. For modeling the beam flanges in the WUF-B specimen, the detailed solid/shell element model used two different

mesh types: (a) a solid element mesh with element size of approximately 4.6 mm, typical of that used in the vicinity of the connections, and (b) a shell element mesh with element size of approximately 19 mm, typical of that used away from the connections. Fig. 2(a) shows the true stress-true strain curves used as input for the beam flange steel for the solid, shell, and beam element models. As is evident in the figure, coarser meshes entail the use of smaller values of ε_f to achieve consistent results. Note that the true stress vs. plastic strain curve used for the shell elements is extrapolated horizontally beyond the point of necking onset, while the curve used for the solid elements is extrapolated tangentially to provide the best match to the tensile test data. Fig. 2(b) presents the measured engineering stress-strain curve from the coupon test samples along with the analysis results of the solid and shell element models of the coupons. Strain values in the figure correspond to a gage length of 51 mm, and results from the beam element model are not included, as they correspond to a longer gage length. The comparison between the measured and calculated stress-strain behavior indicates that the material models capture the constitutive relationships for the steel of the beam flange with reasonable accuracy. The process shown here was repeated for all coupon tests to develop the constitutive material models for all steels used in the specimens corresponding to the various element types and sizes considered in the finite element models. For the reduced models, in which wide flange sections were represented by beam elements, material models were based on stress-strain data from the flanges, rather than the webs.

High Strength Bolts

The bolts connecting the shear tabs to the beam webs in the WUF-B specimen were 25 mm diameter ASTM A490 high strength bolts. In the detailed model of the WUF-B specimen, the bolts were represented using solid elements with a piecewise linear plasticity material model

(material model 24 in LS-DYNA; Hallquist 2007), which was also used for the steel sections and plates. The stress-strain relationship for the bolt material was calibrated to match experimental data reported in Kulak et al. (1987) using a solid element model of a double-shear bolt test. The finite element mesh used to model the bolt in the double-shear test was identical to that used in the detailed model of the WUF-B specimen. Due to symmetry, only one half of the double-shear test specimen was considered in the analysis, with appropriate boundary conditions on the plane of symmetry. Prestressing of the bolts was not considered in this computational study as test data (see Section 4.2.2 of Kulak et al. 1987) and additional analyses showed that prestressing slightly affects the initial response of the bolt in shear, but does not significantly affect the ultimate behavior or fracture of the bolt. In this model, contact was defined between the bolt and the plates to model the transfer of forces through the bolted connection, including friction and bolt bearing. Fig. 3(a) shows the calculated load-deformation curve along with the experimental data from Kulak et al. (1987), while Fig. 3(b) shows a section view of the finite element model at the ultimate load. Fig. 3(c) shows the solid element mesh of the bolt after fracture. Note that the load values reported in Fig. 3(a) are for single shear. For the calculated shear load-deformation curve, the deformations reported are those for the bolt only (between the bolt head and shank), whereas the experimental data includes the test jig deformations. That may explain the difference in elastic stiffness between the measured and calculated responses. Overall, the agreement between the measured and calculated responses was good.

In the reduced model of the WUF-B specimen, spring elements were used to represent the shear behavior of the bolts, along with bearing-induced deformations of the shear tab and beam web, using the piecewise linear shear load-deformation curve shown in Fig. 4(a). This simplified piecewise-linear curve is based on the results of a detailed solid-element model of the

bolted lap joint illustrated in Fig. 4(b), and the shear load-deformation curve obtained from this model is also shown in Fig. 4(a). The two plates in this model correspond to the shear tab and the beam web used in the detailed model of the WUF-B specimen, which are about half as thick as the plates used in the double-shear test [see Fig. 3(b)]. Note that the failure displacement obtained from this single-shear model is more than twice the failure displacement obtained from the double-shear model considered previously (Fig. 3), due largely to more extensive bearing-induced deformations of the thinner plates, which also permitted rotation of the bolt shank. These effects are evident in Fig. 4(b).

Panel Zones

While shear deformations of the panel zones were modeled explicitly in the detailed models, using solid or shell elements, spring elements were used to represent the shear behavior of the panel zones in the reduced models. Diagonal springs representing the panel zones had an elastic, perfectly plastic load deformation curve based on the stiffness and strength of the panel zone (Khandelwal et al. 2008). The stiffness of the panel zone spring, k_{pz} , was defined using equilibrium relationships that equate the response of the panel zone spring model with the column web in the panel zone region deforming in pure shear as:

$$k_{pz} = \frac{G(d_c - t_{cf})t_{pz}}{(d_b - t_{bf})\cos^2 \theta} \quad (1)$$

where d_c is the column depth, d_b is the beam depth, t_{cf} is the column flange thickness, t_{bf} is the beam flange thickness, t_{pz} is the panel zone thickness, θ is the inclination angle of the diagonal spring from the horizontal, and G is the shear modulus of steel. Using similar equilibrium relationships and using the panel zone strength equation in the AISC Seismic Provisions (AISC 2005), the yield capacity of the panel zone spring is:

$$f_{pz} = \frac{0.6F_y d_c t_{pz}}{\cos \theta} \left[1 + \frac{3b_{cf} t_{cf}^2}{d_b d_c t_{pz}} \right] \quad (2)$$

Where b_{cf} is the column flange width. Since the panel zone region is very ductile, it is unlikely that it will fail prior to other components in the model. Therefore, a failure deformation limit on the panel zone spring was not enforced.

Diagonal Braces

In the experimental setup for both specimens (see Lew et al. 2012), two diagonal braces were rigidly attached to the top of each end column to simulate the bracing effect provided by the upper floor framing system in a multi-story building. Since the details of the brace and its connections were not of primary importance to the computational effort, these diagonal braces were represented using an arrangement of spring elements in all models. The load-deformation characteristics of these springs, for each specimen, were estimated based on the axial force and axial displacement (or shortening) of each brace determined from the experiment (see Sadek et al. 2010). Fig. 5 shows the load-deformation curves used to represent the diagonal braces for each specimen. Nonlinear behavior of the braces is evident, most likely associated with yielding and slippage where the braces were connected to the strong floor of the testing facility.

Finite Element Models of WUF-B Specimen

Two finite element models of the WUF-B specimen were developed to study the response characteristics of the specimen and to compare the calculated response with that measured during the test. The first was a detailed model of the specimen with approximately 300 000 solid and shell elements, while the second was a reduced model with about 150 beam and spring elements. The following sections provide descriptions of the models and the analysis results.

Detailed Model

An overview of the detailed model used in the analysis of the WUF-B specimen is shown in Fig. 6(a). Due to symmetry, only one half of the beam-column assembly with appropriate boundary conditions was modeled. The detailed model consisted of finely meshed solid (brick) elements representing the beams, columns, continuity plates, shear tabs, bolts, and welds in the vicinity of the connection [see Fig. 6(b)]. Four layers of solid elements were used for all beam and shear tab plates and welds, which resulted in an element size in the range of 2.8 mm to 4.8 mm. Two to four layers of solid elements were used for all column and continuity plates, which resulted in an element size in the range of 5.6 mm to 13.5 mm. Solid elements with a minimum dimension of 1.8 mm were used for the bolts. Contact was defined between the bolts, shear tabs, and beam webs to model the transfer of forces through the bolted connection, including friction and bolt bearing. Hand calculations showed that the stresses in the fillet weld connecting the shear tab to the column flange were low compared to their strength. As a result, the shear tab was modeled as rigidly connected to the column flange. In addition, no weld-induced residual stresseses were considered for the CJP groove welds between the beam flanges and column flanges. Such residual stresses could potentially lead to earlier yielding of the beam flange, but the ultimate axial and flexural capacities of the section would not be altered (see Section 3.1.3.2 of Bruneau et al. 2011).

Away from the connection zones, the beam and columns were modeled with shell elements (see Fig. 6). Appropriate constraints were imposed at the interface between the shell and solid elements to ensure that nodes on the solid elements remained in the same direction as the fiber of the shell elements. Spring elements were used to model the diagonal braces at the top of the end columns, using the nonlinear load-displacement curve shown in Fig. 5. All nodes

were fixed at the bases of the end columns. Similar to the test configuration, out-of-plane lateral displacements of the beam flanges were constrained at mid-span.

The deflected shape of the WUF-B specimen based on this analysis is shown in Fig. 7(a). The beam remained essentially elastic between connections, as evidenced by the nearly linear displacement profile of the beam span in Fig. 7(a). Plastic deformations, including axial extension and flexural deformation, were concentrated in the connection regions, where significant yielding was observed, as illustrated by the contours of plastic strain shown in Fig. 7(b) for the connection to the center column. The failure mode of the connection in the analysis, shown in Fig. 7(b), was very similar to that observed in the experiment (see Lew et al. 2012). The lowermost bolt connecting the beam web to the shear tab at the center column failed in shear at a vertical displacement of the center column of about 445 mm, which was immediately followed by failure of the middle bolt. The bottom flange of the beam near the weld access hole began to fracture at a center column vertical displacement of approximately 483 mm. The fracture initiated at the root of the access hole (center of flange) and propagated outward until the bottom flange completely fractured.

Reduced Model

The reduced model of the WUF-B specimen, shown in Fig. 8, used Hughes-Liu beam elements (Hallquist 2007) to represent the beams and columns, as well as the shear tabs and beam flanges in the connection regions. The beam elements used cross section integration with the proper cross-sectional geometry defined for each component. A piecewise linear plasticity model was used to represent the steel materials, with stress-strain curves based on tensile test data and fracture modeled using element erosion, as discussed before. An arrangement of beam and spring elements connected with rigid links was used to model the WUF-B connections, as shown in the

figure. Zero-length spring elements (shown with finite length in Fig. 8 for clarity) were used to model the single shear behavior of the bolts, including bearing-induced deformations of the shear tab and beam web, using the load-displacement curve shown in Fig. 4(a). These elements are capable of representing bolt shear in any direction in the vertical plane, allowing modeling of combined vertical and horizontal shear. Spring elements were also used to model the diagonal braces (see Fig. 5) and the shear behavior of the panel zone [Eqs. (1) and (2)].

Two analyses were conducted in which the bases of the end columns were modeled as either fixed or pinned, representing limiting cases for the column fixity. The deflected shape of the WUF-B specimen based on the reduced model with fixed column bases is shown in Fig. 9(a), while the corresponding failure sequence of the center column connection is indicated in Fig. 9(b). The lowermost bolt connecting the beam web to the shear tab failed first, and was followed by the nearly simultaneous failures of the middle bolt and the bottom flange of the beam. This failure sequence is very similar to what was observed in both the experiment and the detailed model.

Comparison with Experimental Measurements

Fig. 10 shows (a) the applied vertical load, (b) the beam axial force, (c) the horizontal (inward) displacement of the end columns at beam mid-height, and (d) the end column axial force, all plotted against the vertical displacement of the center column. These plots compare the results of the detailed and reduced finite element models with experimental measurements described in the companion paper (Lew et al. 2012), showing good agreement between the experimental and computational results. While the reduced model uses far fewer elements than the detailed model, the results show that it is capable of capturing the primary response characteristics of the test specimen.

Consistent with the experimental results, the results of the detailed and reduced models shown in Fig. 10(a) indicate that the assembly remained in the elastic range up to a vertical displacement of the center column of about 50 mm. The analyses indicate that in the early stages of the response the behavior was dominated by flexure, as indicated by the axial compression in the beams shown in Fig. 10(b). With increased vertical displacement, axial tension developed in the beams and the behavior was dominated by catenary action. The axial tensile force in the beams increased with increased downward displacement of the center column, as Fig. 10(b) indicates, until the connection could no longer carry the combined axial and flexural stresses, resulting in the failure of the assembly. The development of axial tension in the beams was associated with increased inward displacement of the end columns at beam mid-height, as shown in Fig. 10(c). Similar to the experimental results, the results of the detailed and reduced models shown in Fig. 10(d) indicate that in the initial stages of the response, the end columns were in compression, but with increased vertical displacement, axial tension developed in the end columns, as a result of the large compressive axial loads carried by the diagonal braces.

Fig. 11 shows the bending moment-axial force interaction diagram for the WUF-B connection, based on the results of the detailed and reduced models. For the reduced model, only the results with fixed column bases are presented for clarity, because the results with pinned column bases are almost indistinguishable. The bending moment and axial force were calculated at the face of the center column, where failure of the connection was observed. Superimposed on the connection response are the limiting bending moment-axial tension interaction diagrams for the gross beam cross section (W21x73) calculated based on the actual yield and ultimate strengths of the beam material. The limiting interaction diagrams for the beam cross section were calculated based on Chapter H of the 2005 AISC Specification (AISC 2005). The figure

shows that the capacity of the WUF-B connection exceeds the yield capacity of the beam gross cross section under combined axial and flexural loads, but is somewhat less than the ultimate strength of the beam.

Finite Element Models of RBS Specimen

Similar to the WUF-B specimen, two finite element models of the RBS specimen were developed to study the response characteristics of the connections and to compare the calculated response with that measured during the experiment. The first was a detailed model of the assembly with approximately 235 000 shell elements, while the second was a reduced model with about 130 beam and spring elements. The following sections provide descriptions of the models and the analysis results.

Detailed Model

An overview of the detailed model used in the analysis of the RBS specimen is shown in Fig. 12. The model consisted of shell elements representing the columns, beams, continuity and doubler plates, and welds. In the vicinity of the reduced section, the beams and columns were modeled using a fine shell element mesh with an element size of about 6.4 mm. Away from the connection zones, the beams and columns were modeled using a coarser mesh with an element size of 25 mm. Spring elements were used to model the diagonal braces at the top of the end columns, using the nonlinear load-displacement curve shown in Fig. 5. All nodes were fixed at the bases of the end columns. Similar to the test configuration, out-of-plane lateral displacements of the beam flanges were constrained at mid-span.

The deflected shape of the RBS specimen based on the detailed analysis is shown in Fig. 13(a). Only half of the model is shown in Fig. 13(a) because of the symmetry of the deflected

shape. The beams remained essentially elastic between the reduced sections, as evidenced by the nearly linear displacement profile of the beam span in Fig. 13(a). Plastic deformations, including axial extension and flexural deformation, were concentrated in the reduced sections, where significant yielding was observed, as illustrated by the contours of plastic strain shown in Fig. 13(b) for the reduced section near the center column. The failure mode from the analysis, shown in Fig. 13(b), was very similar to that observed in the experiment (see Lew et al. 2012). The failure was characterized by the fracture of the bottom flange in the reduced section near the center column, which displaced about 838 mm. The fracture immediately propagated through the web until the vertical load-carrying capacity of the specimen was lost.

Reduced Model

The reduced model of the RBS specimen, shown in Fig. 14, consisted of Hughes-Liu beam elements representing the beams and columns in the specimen. In addition, each reduced beam section was modeled using five beam elements with varying section properties. The beam elements used cross section integration with the proper cross-sectional geometry defined for each type of section. A piecewise linear plasticity model was used to represent the steel materials, with stress-strain curves based on tensile test data and fracture represented using element erosion, as discussed earlier. Spring elements were used to model the diagonal braces (Fig. 5) and the shear behavior of the panel zone [Eqs. (1) and (2)]. Both fixed and pinned bases were considered for the end columns.

In general, the results from the reduced model were consistent with those from the detailed model. The deflected shape of the RBS specimen based on the reduced model with fixed column bases is shown in Fig. 15. The failure mode of the specimen based on the reduced model (for both fixed and pinned end columns) was consistent with that observed in the

experiment and the detailed model. The beam element at the center of the reduced section experienced large strains, associated with combined flexural and axial tensile stresses. Once a critical strain was reached, the element was eroded, resulting in the failure of the assembly.

Comparison with Experimental Measurements

Figs. 16 and 17 compare the results from the detailed and reduced finite element models with experimental measurements described in the companion paper (Lew et al. 2012). Fig. 16 shows (a) the applied vertical load, (b) the beam axial force, (c) the end column axial force, and (d) the axial compression in each diagonal brace, all plotted against the vertical displacement of the center column. Fig. 17 shows the horizontal (inward) displacement of the end columns at (a) beam mid-height and (b) the top of the end columns, also plotted against the vertical displacement of the center column. Good agreement is observed between the experimental and computational results, and the results show that the reduced model, with far fewer elements than the detailed model, is able to capture the primary response characteristics of the test specimen. The reduced model results with fixed and pinned column bases generally bracket the experimental results.

Consistent with the experimental results, the results of the detailed and reduced models shown in Fig. 16(a) indicate that the assembly remained in the elastic range up to a vertical displacement of the center column of about 50 mm. The analyses indicate that in the early stages of the response, the behavior was dominated by flexure, as indicated by the slight compressive axial forces in the beams shown in Fig. 16(b). With increased vertical displacement, tensile axial forces developed in the beams and the behavior was dominated by catenary action. As Fig. 16(b) indicates, the axial tensile force in the beams increased with increased downward displacement of the center column until the connection could no longer carry the combined axial and flexural

stresses, resulting in fracture of the bottom flange at the center of the reduced section. Similar to the experimental results, the results of the detailed and reduced models shown in Fig. 16(c) indicate that in the initial stages of the response (when the response was dominated by flexure), the end columns were in compression. With increased vertical displacement, axial tension developed in the end columns as a result of the large compressive axial loads carried by the diagonal braces, as shown in Fig. 16(d). The development of axial tension in the beams was associated with increased inward displacement of the end columns at beam mid-height, as shown in Fig. 17.

Fig. 18 shows the bending moment-axial force interaction diagram for the RBS connection, based on the detailed and reduced models. For the reduced model, only the results with fixed column bases are presented for clarity, because the results with pinned column bases are very similar. The bending moment and axial force were calculated at the center of the reduced section near the center column, where failure of the connection was observed. Superimposed on the connection response are the limiting bending moment-axial tension interaction diagrams for the gross beam cross section (W24x94) and for the reduced beam section calculated based on the actual ultimate strength of the beam material. The limiting interaction diagrams were calculated based on Chapter H of the 2005 AISC Specification (AISC 2005) using yield and ultimate stress values obtained from coupon tensile tests. The figure shows that the capacity of the connection slightly exceeds the capacity of the reduced section under combined axial and flexural loads, as calculated based on the AISC Specification, but is less than the calculated ultimate capacity of the gross beam cross section.

Influence of Column Restraint Conditions

In the test setup for both assemblies, illustrated in Fig. 19(a), diagonal braces were used to provide lateral restraint to the column tops to enable the development of catenary action. These braces were intended to represent the lateral restraint provided in a configuration similar to that illustrated in Fig. 19(b). In this configuration, the end columns extend one story (4.19 m) above and below the beam level, and the tops and bottoms of the end columns are fixed to represent the restraint provided by the upper and lower floor framing systems. To assess how closely the test setup in Fig. 19(a) represents the configuration in Fig. 19(b), both the WUF-B and RBS assemblies were analyzed in the configuration of Fig. 19(b) using the reduced models developed in this study. Fig. 20 shows the vertical load versus the vertical displacement of the center column for (a) the WUF-B assembly and (b) the RBS assembly in the two configurations shown in Fig. 19. For both the WUF-B and the RBS assemblies, good agreement is observed between the results computed for the two configurations, confirming that the column restraint conditions in the two configurations yield consistent results.

Summary and Conclusions

This paper presented a computational assessment of the performance of beam-column assemblies with two types of moment connections under vertical column displacement. The connections considered include a welded unreinforced flange-bolted web (WUF-B) connection and a reduced beam section (RBS) connection. The study considered two levels of modeling complexity: (1) detailed models with a large number of elements, primarily solid and shell elements, and (2) reduced models with a limited number of elements, primarily beam and spring elements. The analyses conducted using these models provided insight into the behavior and failure modes of the connections, including their capacity to sustain tensile forces that developed in the beams.

For both the WUF-B and RBS assemblies, the analyses showed an initial elastic response dominated by flexural behavior. With increased vertical displacement, yielding occurred at the beam-to-column connections, and axial tension developed in the beams. The analyses confirm that the moment connections are able to sustain significant axial forces after the formation of plastic hinges and thus to resist the applied vertical loads through catenary action. The ultimate fracture of the connections in both assemblies was due to combined axial and flexural stresses associated with increasing axial tension in the beams. Comparison of the computed bending moment and axial force values with the interaction equation for the beam cross sections showed that the moment connections are capable of developing a significant fraction of the cross-sectional capacity of the beams under combined axial and flexural loads.

Comparison of the computational results with experimental measurements described in the companion paper showed good agreement. Both detailed and reduced models were capable of capturing the primary response characteristics and failure modes, providing validation of the modeling approaches. The reduced models developed in this study will be valuable in the analysis of complete structural systems for assessing the reserve capacity and robustness of building structures.

Disclaimer

Certain commercial entities, equipment, products, or materials are identified in this document in order to describe a procedure or concept adequately. Such identification is not intended to imply recommendation, endorsement, or implication that the entities, products, materials, or equipment are necessarily the best available for the purpose.

References

- Alashker, Y., El-Tawil, S. and Sadek, F. (2010). "Progressive Collapse Resistance of Steel-Concrete Composite Floors." *Journal of Structural Engineering*, 136(10), 1187-1196.
- Alashker, Y., Li, H. and El-Tawil, S. (2011). "Approximations in Progressive Collapse Modeling." *Journal of Structural Engineering*, (in press).
- American Institute of Steel Construction (AISC). (2005). "Seismic Provisions for Structural Steel Buildings, Including Supplement No. 1." Chicago, IL.
- American Institute of Steel Construction (AISC). (2005). "Specification for Structural Steel Buildings." *ANSI/AISC 360-05*, Chicago, IL.
- ASTM. (2003), "Standard Test Methods and Definitions for Mechanical Testing of Steel Products." *ASTM A370 – 03a*, ASTM International, West Conshohocken, PA.
- Bruneau, M., Uang, C.M., and Sabelli, R. (2011). *Ductile Design of Steel Structures*, Second Edition, McGraw-Hill, New York.
- Del Savio, A.A., Nethercot, D.A., Vellasco, P.C.G.S, Andrade, S.A.L., and Martha, L.F. (2009). "Generalized component-based model for beam-to-column connections including axial versus moment interaction." *Journal of Constructional Steel Research*, 65, 1876-1895.
- Hallquist, J. (2007). "LS-DYNA Keyword User's Manual." Livermore Software Technology Corporation, Livermore, CA.
- Khandelwal, K. and El-Tawil, S. (2007). "Collapse behavior of steel special moment resisting frame connections." *Journal of Structural Engineering*, 133(5), 646-655.
- Khandelwal, K., El-Tawil, S., Kunnnath, S.K., Lew, H.S. (2008). "Macromodel-based simulation of progressive collapse: steel frame structures." *Journal of Structural Engineering*, 134(7), 1070-1078.
- Khandelwal, K., El-Tawil, S., Sadek, F. (2009). "Progressive collapse analysis of seismically designed steel braced frames." *Journal of Constructional Steel Research*, 65, 699-708.
- Khandelwal, K. and El-Tawil, S. (2011). "Pushdown resistance as a measure of robustness in progressive collapse analysis," *Engineering Structures*, (in press).

Kulak, G. L., Fisher, J. W., and Struik, J. H. A., (1986). *Guide to Design Criteria for Bolts and Riveted Joints*, 2nd Ed., John Wiley & Sons, New York.

Lew, H. S., Main, J. A., Robert, S. D., Sadek, F., and Chiarito, V. P., (2012). "Performance of steel moment connections under a column removal scenario. I: Experiments." submitted to *Journal of Structural Engineering*.

Sadek, F., El-Tawil, S., and Lew, H.S. (2008). "Robustness of composite floor systems with shear connections: modeling, simulation, and evaluation." *Journal of Structural Engineering*, 134(11), 1717-1725.

Sadek, F., Main, J. A., Lew, H. S., Robert, S. D., Chiarito, V. P., and El-Tawil, S. (2010). "An Experimental and Computational Study of Steel Moment Connections under a Column Removal Scenario." *NIST Technical Note 1669*, National Institute of Standards and Technology, Gaithersburg, MD.

Yim, H.C. and Krauthammer, T. (2010). "Mathematical-mechanical model of WUF-B connection under monotonic load." *Engineering Journal*, 47(2), 71-90.

List of Figures

- Fig. 1 Sample finite element models of tensile coupons: (a) solid elements; (b) shell elements
- Fig. 2 (a) True stress-strain curves for the solid, shell, and beam elements and (b) engineering stress-strain curves from coupon models and tests (beam flange steel from WUF-B specimen)
- Fig. 3 (a) Measured and calculated shear load-deformation curves for 25 mm A490 bolt; (b) section view of finite element model showing deformations at ultimate load
- Fig. 4 (a) Shear load-deformation curves for bolted lap joint; (b) section view of finite element model showing deformations at ultimate load
- Fig. 5 Axial load-displacement curve for diagonal braces for WUF-B and RBS specimens
- Fig. 6 Detailed model of WUF-B specimen: (a) overview; (b) connection to center column
- Fig. 7 Detailed model results for WUF-B specimen: (a) deflected shape at a center column displacement of 512 mm; (b) failure mode at connection to center column
- Fig. 8 Reduced model of WUF-B specimen: (a) overview; (b) connections to center column
- Fig. 9 Results from reduced model of WUF-B specimen (fixed columns): (a) deflected shape at a center column displacement of 511 mm; (b) failure sequence at connection to center column
- Fig. 10 (a) Applied vertical load, (b) beam axial force, (c) horizontal displacement of end column at beam mid-height, and (d) end column axial force versus center column displacement for WUF-B specimen (estimated coefficient of variation in measurements: 1 %)
- Fig. 11 Axial load versus bending moment for WUF-B connection to center column
- Fig. 12 Detailed model of RBS specimen: (a) overview; (b) reduced beam section near connection to center column
- Fig. 13 Detailed model results for RBS specimen: (a) deflected shape at a center column displacement of 875 mm; (b) failure mode in reduced section near center column

- Fig. 14 Reduced model of RBS specimen: (a) overview; (b) connection to center column showing reduced beam section
- Fig. 15 Deflected shape from reduced model of RBS specimen (fixed columns) at a center column displacement of 867 mm
- Fig. 16 (a) Applied vertical load, (b) beam axial force, (c) column axial force, and (d) axial compression in brace versus center column displacement for RBS specimen (estimated coefficient of variation in measurements: 1 %)
- Fig. 17 Horizontal displacement of end column at (a) beam mid-height and (b) column top versus center column displacement for RBS specimen (estimated coefficient of variation in measurements: 1 %)
- Fig. 18 Beam axial load versus bending moment for reduced beam section near center column
- Fig. 19 Alternate configurations for restraint of end columns: (a) diagonal braces; (b) restraint at upper floor level
- Fig. 20 Influence of column restraint conditions on vertical load versus center column displacement: (a) WUF-B specimen; (b) RBS specimen

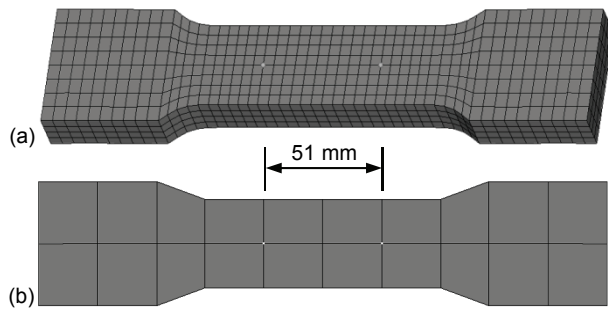


Fig. 1. Sample finite element models of tensile coupons: (a) solid elements; (b) shell elements

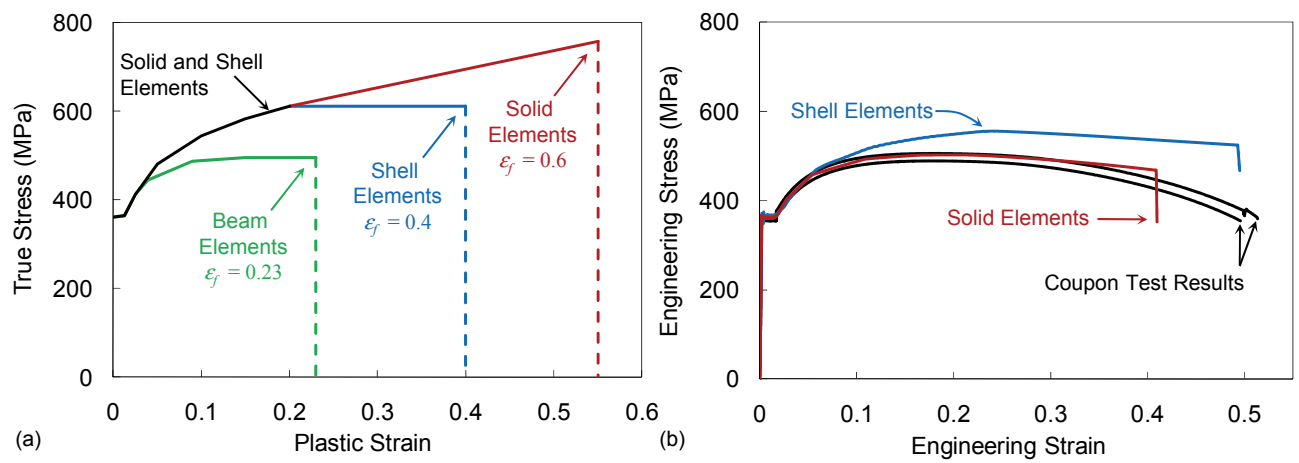


Fig. 2. (a) True stress-strain curves for solid, shell, and beam element models and (b) engineering stress-strain curves from coupon models and tests (beam flange steel from WUF-B specimen)

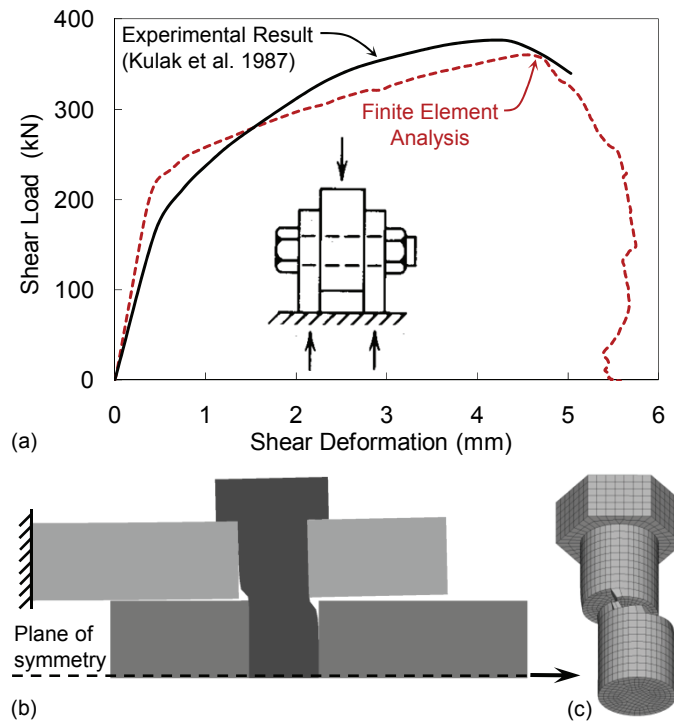


Fig. 3. (a) Measured and calculated shear load-deformation curves for 25 mm A490 bolt;
 (b) section view of finite element model at ultimate load; (c) bolt mesh after fracture

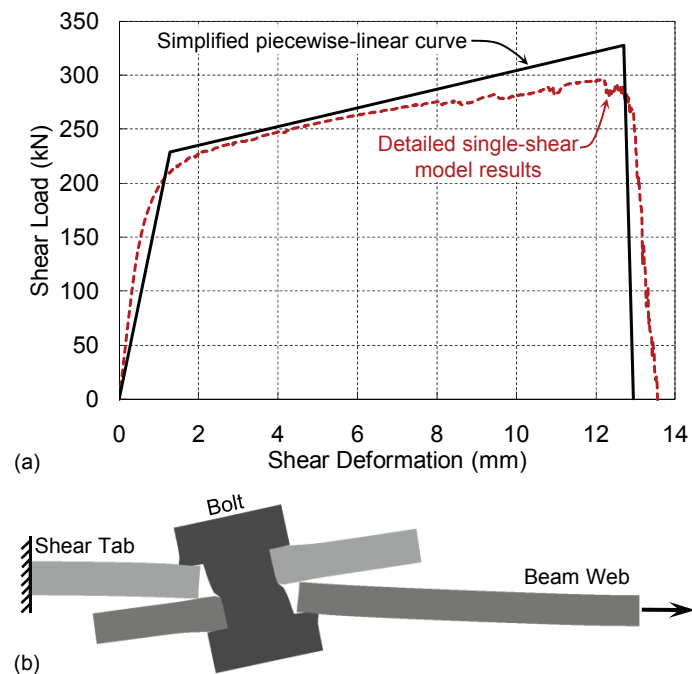


Fig. 4. (a) Shear load-deformation curves for bolted lap joint; (b) section view of finite element model showing deformations at ultimate load

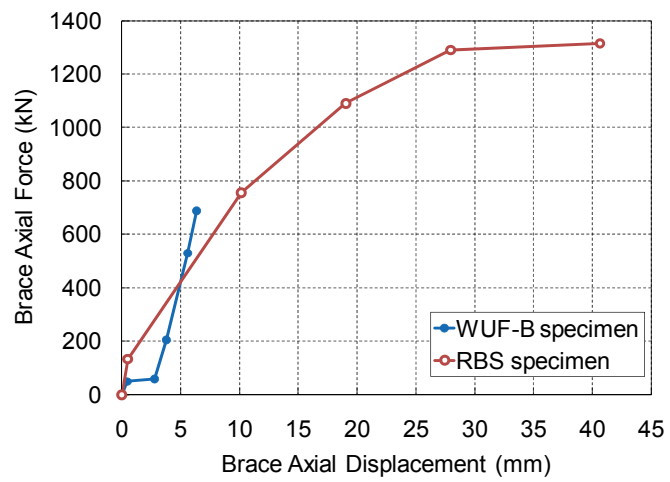


Fig. 5. Axial load-displacement curve for diagonal braces for WUF-B and RBS specimens

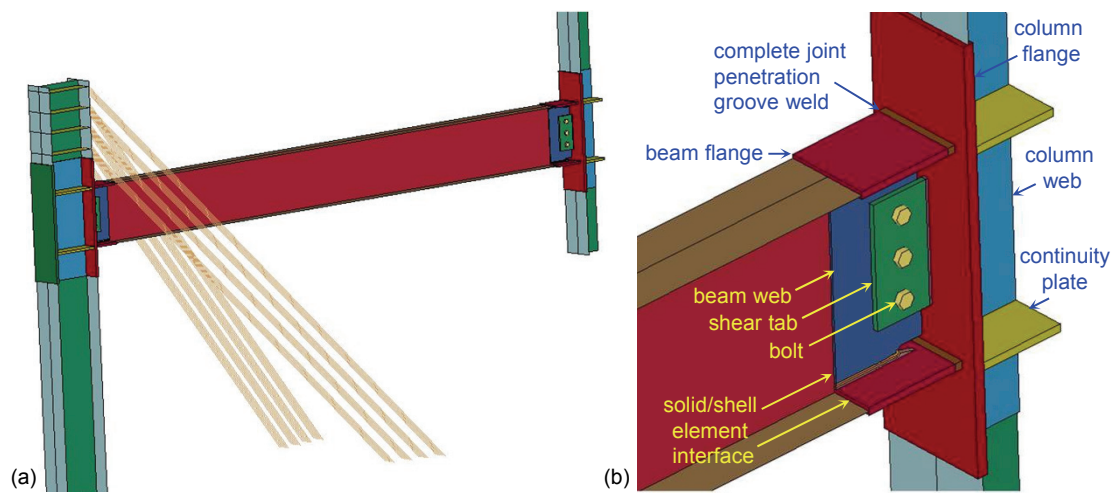


Fig. 6. Detailed model of WUF-B specimen: (a) overview; (b) connection to center column

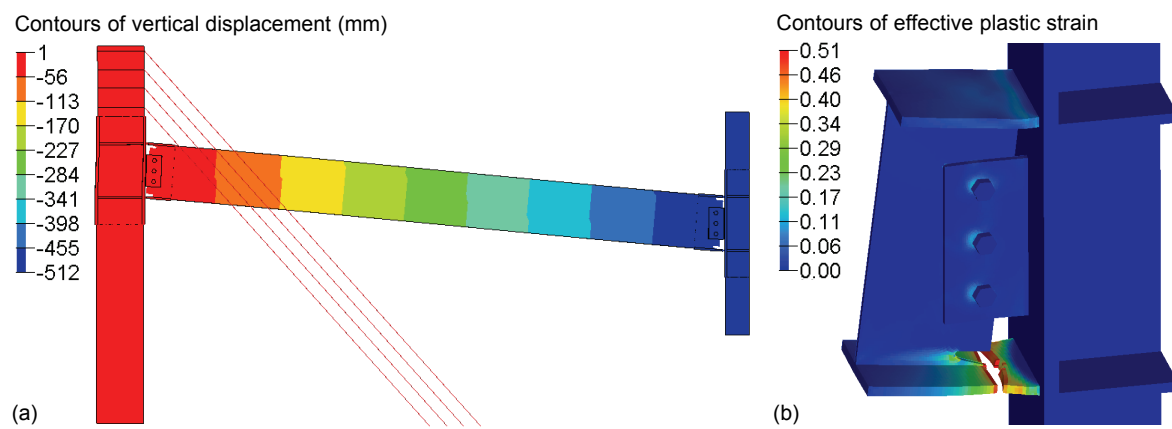


Fig. 7. Detailed model results for WUF-B specimen: (a) deflected shape at a center column displacement of 512 mm; (b) failure mode at connection to center column

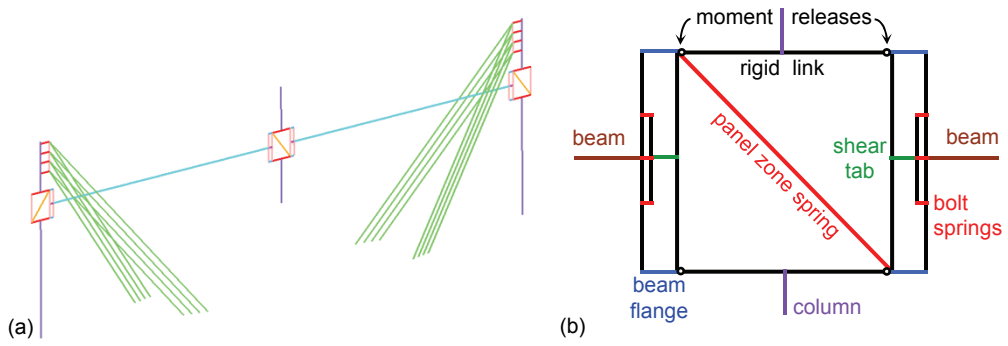


Fig. 8. Reduced model of WUF-B specimen: (a) overview; (b) connections to center column

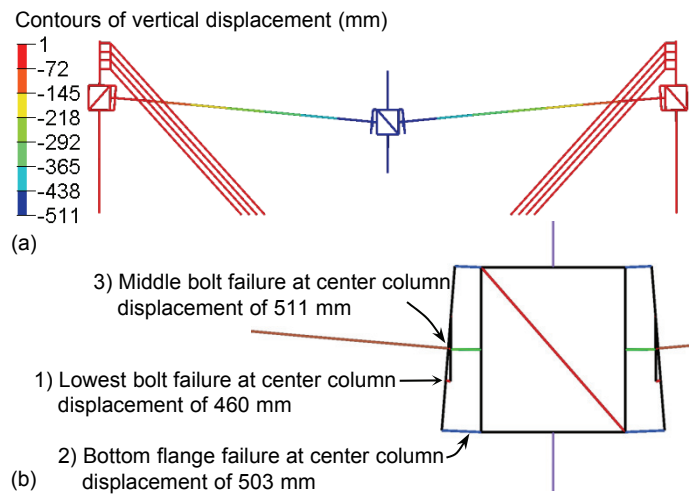


Fig. 9. Results from reduced model of WUF-B specimen (fixed columns): (a) deflected shape at a center column displacement of 511 mm; (b) failure sequence at connection to center column

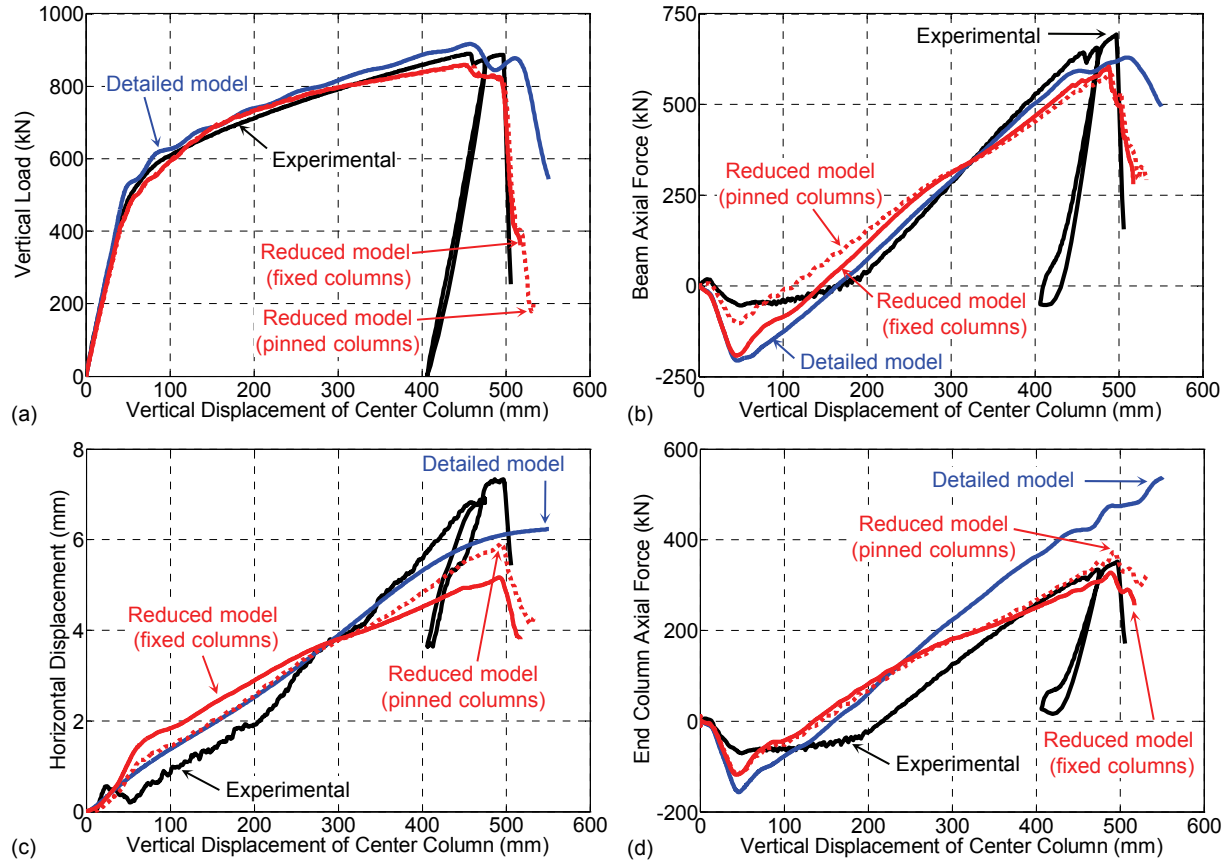


Fig. 10. (a) Applied vertical load, (b) beam axial force, (c) horizontal displacement of end column at beam mid-height, and (d) end column axial force versus center column displacement for WUF-B specimen (estimated coefficient of variation in measurements: 1 %)

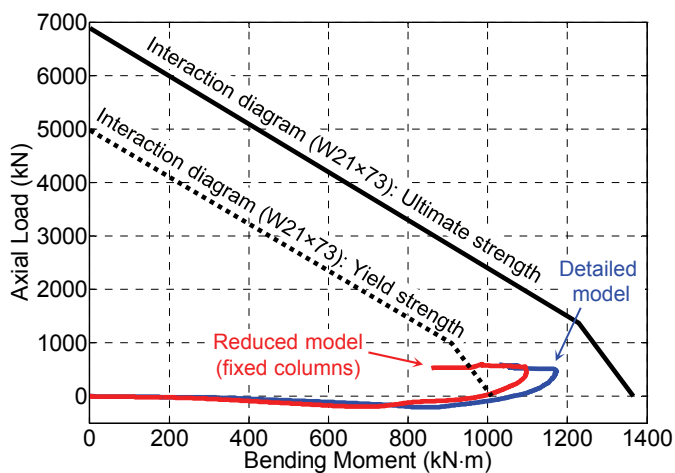


Fig. 11. Axial load versus bending moment for WUF-B connection to center column

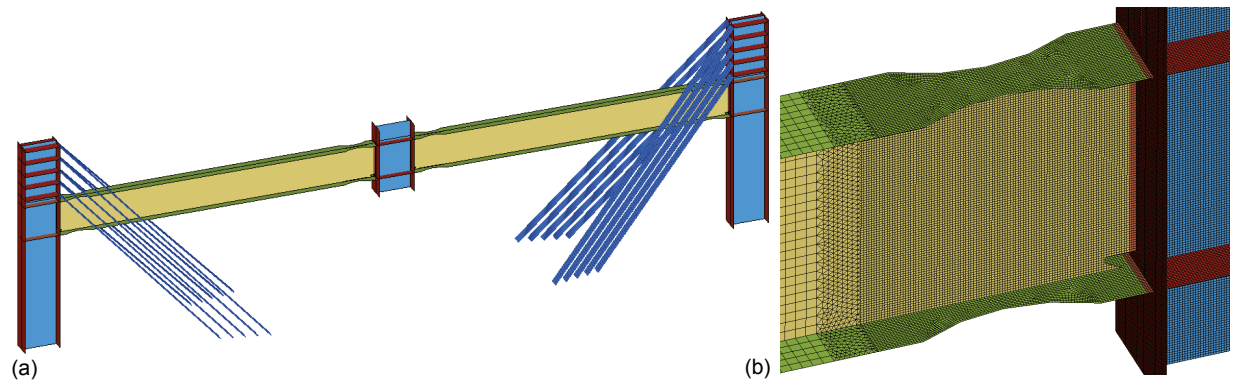


Fig. 12. Detailed model of RBS specimen: (a) overview; (b) reduced beam section near connection to center column

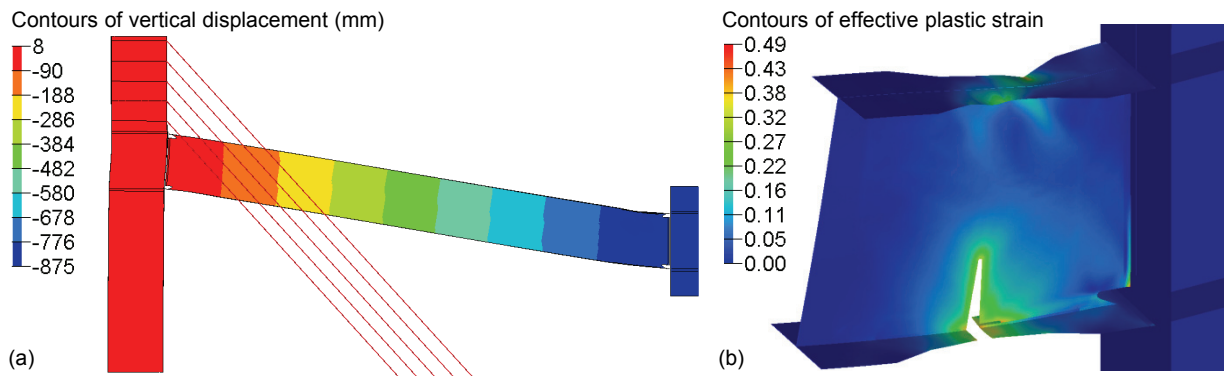


Fig. 13. Detailed model results for RBS specimen: (a) deflected shape at a center column displacement of 875 mm; (b) failure mode in reduced section near center column

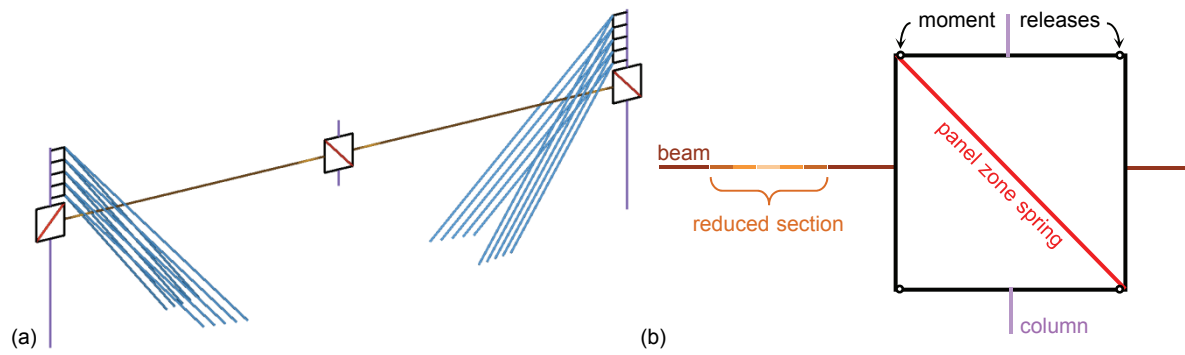


Fig. 14. Reduced model of RBS specimen: (a) overview; (b) connection to center column showing reduced beam section

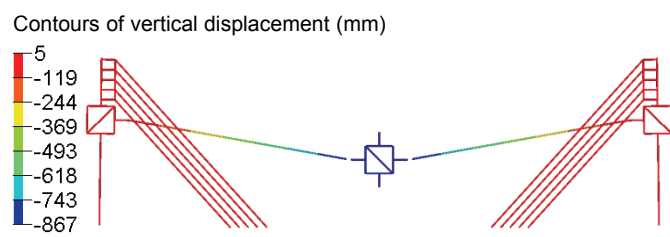


Fig. 15. Deflected shape from reduced model of RBS specimen (fixed columns) at a center column displacement of 867 mm

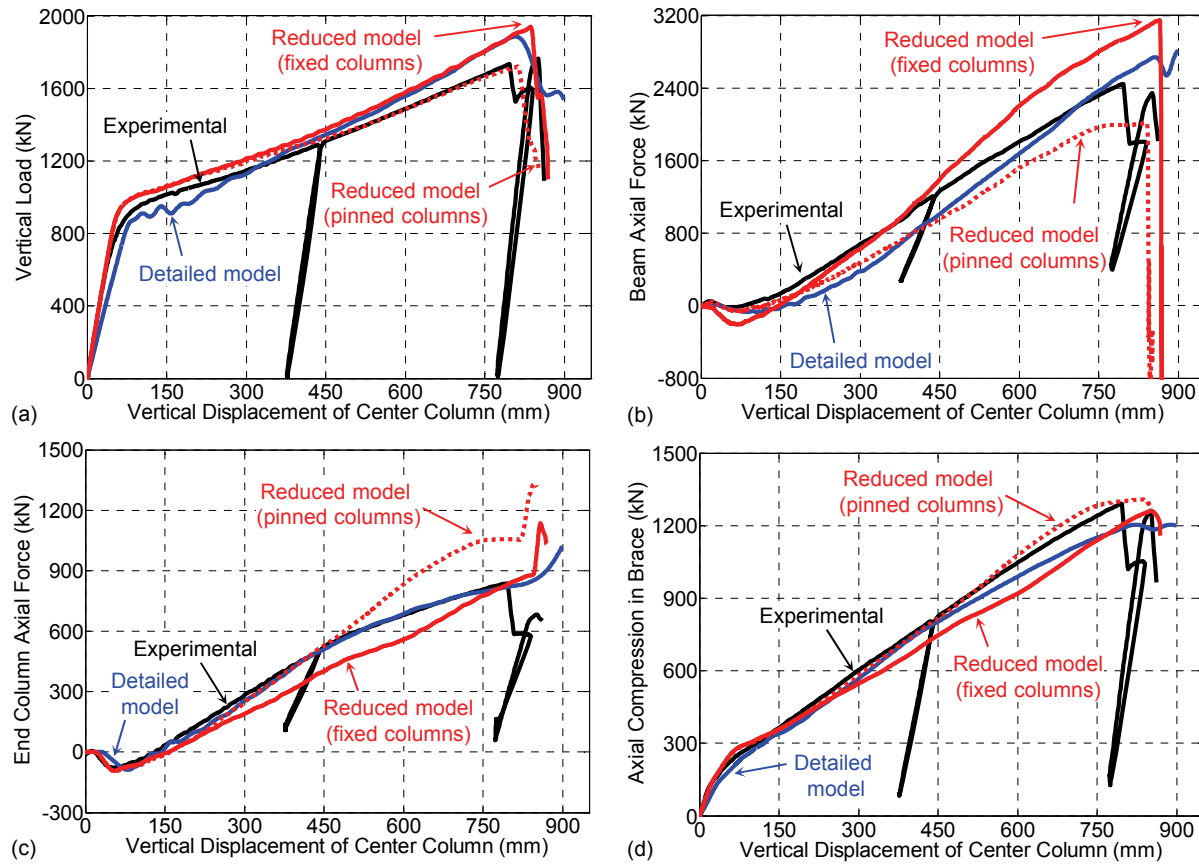


Fig. 16. (a) Applied vertical load, (b) beam axial force, (c) end column axial force, and (d) axial compression in brace versus center column displacement for RBS specimen
(estimated coefficient of variation in measurements: 1 %)

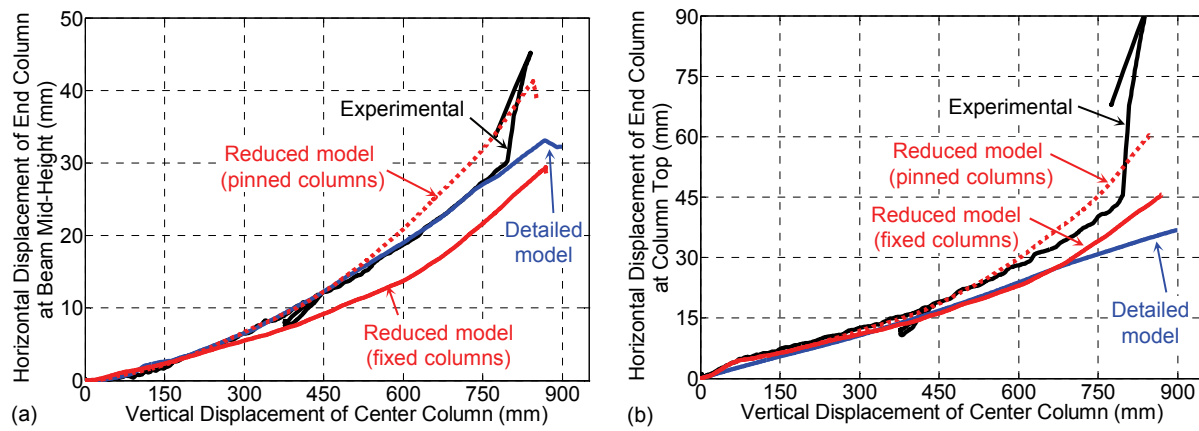


Fig. 17. Horizontal displacement of end column at (a) beam mid-height and (b) column top versus center column displacement for RBS specimen
(estimated coefficient of variation in measurements: 1 %)

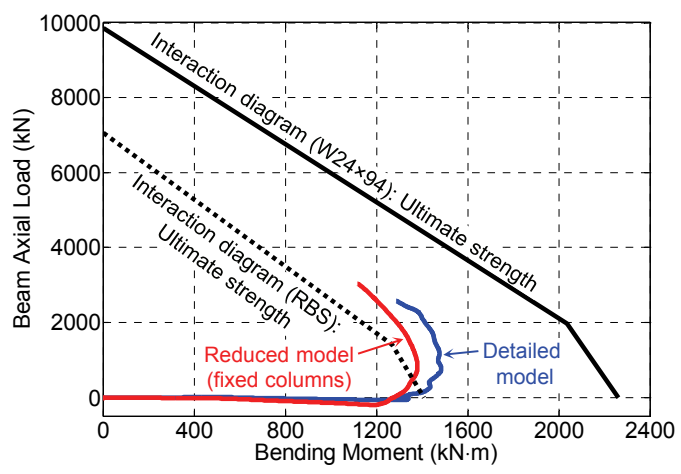


Fig. 18. Beam axial load versus bending moment for reduced beam section near center column

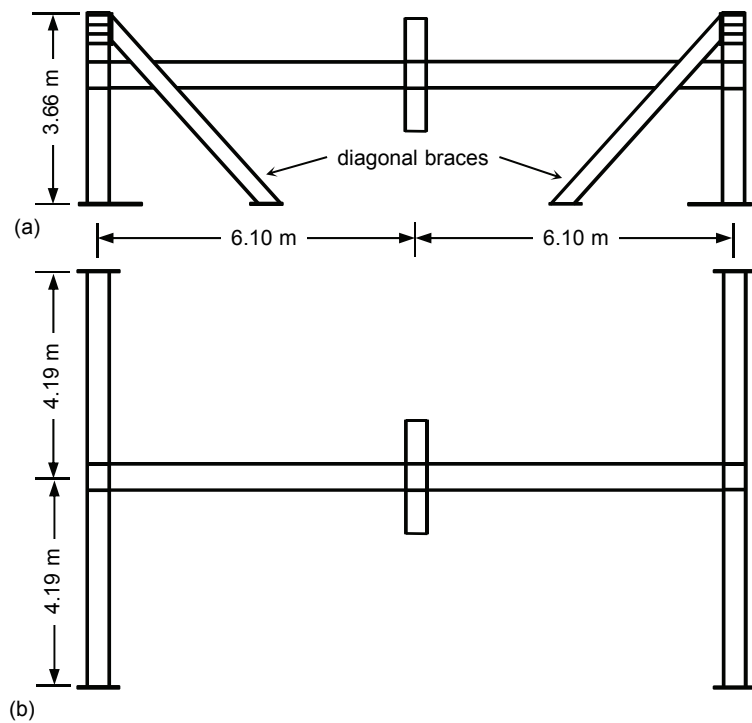


Fig. 19. Alternate configurations for restraint of end columns: (a) diagonal braces; (b) restraint at upper floor level

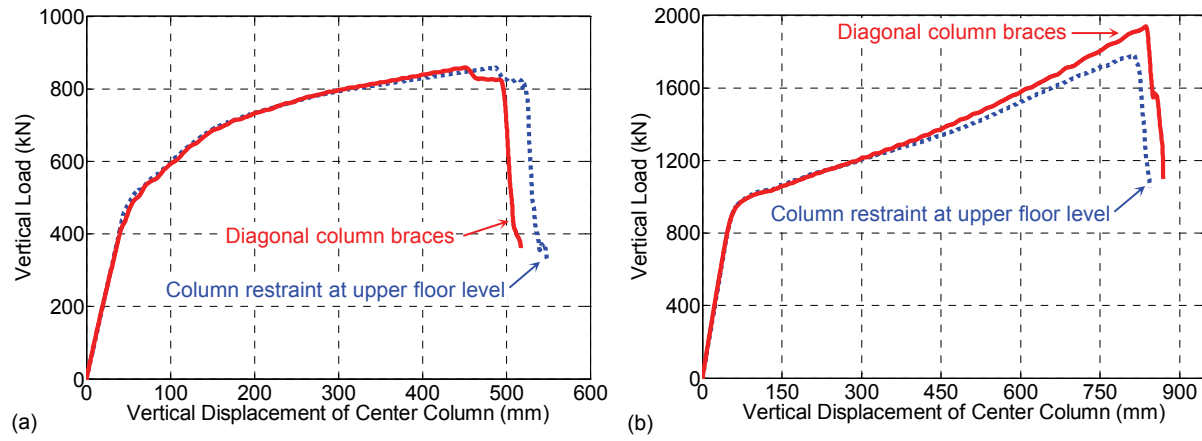


Fig. 20. Influence of column restraint conditions on vertical load versus center column displacement: (a) WUF-B specimen; (b) RBS specimen